

Intrinsic polarization conversion and avoided-mode crossing in X-cut lithium niobate microrings

Zelin Tan(谭泽林), Jianfa Zhang(张检发), Zhihong Zhu(朱志宏), Wei Chen(陈伟), Zhengzheng Shao(邵铮铮), Ken Liu(刘肯), and Shiqiao Qin(秦石乔)

Citation: Chin. Phys. B, 2024, 33 (**6**): 064205. DOI: 10.1088/1674-1056/ad47b2
Journal homepage: http://cpb.iphy.ac.cn; http://iopscience.iop.org/cpb

What follows is a list of articles you may be interested in

High efficiency of broadband transmissive metasurface terahertz polarization converter

Qiangguo Zhou(周强国), Yang Li(李洋), Yongzhen Li(李永振), Niangjuan Yao(姚娘娟), and Zhiming Huang(黄志明)
Chin. Phys. B, 2023, 32 (**2**): 024201. DOI: 10.1088/1674-1056/ac6db7

Transmission-type reconfigurable metasurface for linear-to-circular and linear-to-linear polarization conversions

Ping Wang(王平), Yu Wang(王豫), Zhongming Yan(严仲明), and Hongcheng Zhou(周洪澄)
Chin. Phys. B, 2022, 31 (**12**): 124201. DOI: 10.1088/1674-1056/ac8ce0

Switchable terahertz polarization converter based on VO_2 metamaterial

Haotian Du(杜皓天), Mingzhu Jiang(江明珠), Lizhen Zeng(曾丽珍), Longhui Zhang(张隆辉), Weilin Xu(徐卫林), Xiaowen Zhang(张小文), and Fangrong Hu(胡放荣)
Chin. Phys. B, 2022, 31 (**6**): 064210. DOI: 10.1088/1674-1056/ac4f5b

An ultra-wideband 2-bit coding metasurface using Pancharatnam—Berry phase for radar cross-section reduction

Bao-Qin Lin(林宝勤), Wen-Zhun Huang(黄文准), Lin-Tao Lv(吕林涛), Jian-Xin Guo(郭建新),Yan-Wen Wang(王衍文), and Hong-Jun Ye(叶红军)
Chin. Phys. B, 2022, 31 (**3**): 034204. DOI: 10.1088/1674-1056/ac11ec

A novel polarization converter based on the band-stop frequency selective surface

Kun Liao(廖昆), Shining Sun(孙世宁), Xinyuan Zheng(郑昕原), Xianxian Shao(邵纤纤), Xiangkun Kong(孔祥鲲), and Shaobin Liu(刘少斌)
Chin. Phys. B, 2022, 31 (**2**): 024211. DOI: 10.1088/1674-1056/ac1fdd

---

Intrinsic polarization conversion and avoided-mode crossing in X-cut lithium niobate microrings

Zelin Tan(谭泽林)[1,2], Jianfa Zhang(张检发)[1,2], Zhihong Zhu(朱志宏)[1,2], Wei Chen(陈伟)[3], Zhengzheng Shao(邵铮铮)[4,†], Ken Liu(刘肯)[1,2,‡], and Shiqiao Qin(秦石乔)[1,2,§]

[1] *College of Advanced Interdisciplinary Studies & Hunan Provincial Key Laboratory of Novel Nano Optoelectronic Information Materials and Devices, National University of Defense Technology, Changsha* 410073, *China*

[2] *Nanhu Laser Laboratory, National University of Defense Technology, Changsha* 410073, *China*

[3] *College of Meteorology and Oceanography, National University of Defense Technology, Changsha* 410073, *China*

[4] *School of Physics, Central South University, Changsha* 410083, *China*

(Received 24 April 2024; revised manuscript received 30 April 2024; accepted manuscript online 6 May 2024)

Compared with well-developed free space polarization converters, polarization conversion between TE and TM modes in the waveguide is generally considered to be caused by shape birefringence, like curvature, morphology of waveguide cross section and scattering. Here, we study the polarization conversion mechanism in 1-THz-FSR X-cut lithium niobate microrings with multiple-resonance condition, that is the conversion can be implemented by birefringence of waveguides, which will also introduce an avoided-mode crossing. In the experiment, we find that this mode crossing results in severe suppression of one sideband in local nondegenerate four-wave mixing and disrupts the cascaded four-wave mixing on this side. Simultaneously, we propose one two-dimensional method to simulate the eigenmodes (TE and TM) in X-cut microrings, and the mode crossing point. This work will provide one approach to the design of polarization converters and simulation for monolithic photonics integrated circuits, and may be helpful to the studies of missed temporal dissipative soliton formation in X-cut lithium niobate rings.

Keywords: polarization conversion, birefringence, nondegenerate four-wave mixing

PACS: 42.81.Gs, 52.35.Mw, 42.82.–m **DOI:** 10.1088/1674-1056/ad47b2

1. Introduction

As one of the basic properties of electromagnetic waves, polarization plays important roles in optical communication and detection.[1] Leveraging birefringence of structures, originating from shape or material itself, is the main method to manipulate the polarization, which has been developed well in free space like converters based on metasurfaces.[1–4] However, it remains a challenge to interconnect this kind of converters with other integrated functional devices, which can be handled by fiber,[5] but greatly destroy the miniaturization of integrated circuits. In the waveguide regime, polarization conversion of orthogonal modes, TE and TM, is generally regarded as mode coupling, arising from the curvature, cross-section size, sidewall inclination angle and scattering of the waveguide,[6–10] which can be classified as shape anisotropy. Several papers have demonstrated that polarization coupling or mode hybridization in thin-film lithium niobate (LN) waveguides, however, the essence is not figured out clearly.[11–14] As a result, the potential of birefringent platform, such as lithium niobate (LN), for mode conversion has not been excavated.

In recent years, with the maturity of commercial manufacture of thin-film LN and breakthroughs in low-loss LN waveguide fabrication,[15–21] lithium niobate on insulator (LNOI) has become one of the most attractive platforms for monolithic PIC, due to its excellent nonlinear, acousto–optic, electro–optic characteristics, relatively high refractive index and wide-spectrum transparent window.[22] In practice, to make full use of the excellent properties of LN, such as the second-order nonlinear tensor element d_{33} (-27 pm/V) and Pockels coefficient r_{33} (31 pm/V), devices are usually designed and fabricated on X-cut LN platform. Common structures include Mach–Zehnder interferometer-based modulators capable of ultrafast modulation,[23–25] periodically polarized LN waveguides for wavelength conversion,[26,27] and rings for generating optical frequency combs, etc.[28,29]

Here, by investigating the nondegenerate four-wave mixing (FWM) in an X-cut LN microring, where the birefringence cannot be neglected or avoided, we find that one sideband (blue wavelength) of a pair is suppressed severely with two pumps detuned from blue to effective zero detuning of their corresponding high-Q resonances. The suppressed sideband is released until the third sideband (red wavelength) is generated by cascade FWM. From the resonator transmission spectrum, we find that two mode families (TE and TM) are supported, resulting in avoided-mode crossing between the pump and the

†Corresponding author. E-mail: zzshao_nudt@163.com
‡Corresponding author. E-mail: liukener@163.com
§Corresponding author. E-mail: sqqin8@nudt.edu.cn

© 2024 Chinese Physical Society and IOP Publishing Ltd

first sideband in blue wavelength. Thus, the non-degenerate FWM is disrupted as well as subsequent cascade FWM on this side for heavily distorted dispersion around the crossing position.

The reason for this phenomenon is a hidden mechanism in birefringent waveguides. Because the angle between TE mode polarization and the optical axis (Z axis) changes with light propagation in the ring, the effective index of the TE mode varies with azimuth on the interval $[n_e, n_o]$, where n_e, n_o represent the extraordinary and ordinary index, respectively. For TM mode, its polarization is always perpendicular to the Z axis, so the effective index corresponds to the ordinary index abidingly. This distinction causes the effective indices of these two modes in X-cut LN microrings will cross at certain azimuth, so that modes show strong interaction at these points resulting in polarization conversion, stimulating the TM modes when satisfy the resonance condition. This is inevitable and will disrupt the FWM around the mode-crossing point between TE and TM mode families, which can be eliminated with a special design of ring width and shape.[30] Calculating the eigenmodes as well as mode crossings point in a birefringent microring is not easy, due to the anisotropic nature. At the end of this paper, we propose a 2D-equivalent method, stretching the ring to a straight waveguide with periodic boundaries at both ends, that fits well with experimental results without considering the dispersion.

2. Results and discussion

Figure 1(a) shows the experimental setup for nondegenerate FWM. Two continuous wave (CW) lasers with different wavelengths ($\sim$ 1602 nm, $\sim$ 1594 nm) and same power ($\sim$ 4 mW) are coupled into the waveguide through the polarization controller and fiber coupler successively. The inset in Fig. 1(a) shows a schematic cross-section of the waveguide. In this experiment, an X-cut LN microring is fabricated by Ar^+ ion. A total of 615 nm of LN is etched, leaving a 75 nm thick slab. The waveguide sidewall tilt angle is 77°. The ring radius is 23 μm, corresponding to a free spectral range (FSR) of $\sim$ 1 THz. When the CW pump is coupled into the cavity modes, the cavity absorbs a small fraction of the energy and is heated up. Elevated temperature will change the effective refractive index of the cavity mode, shifting the resonance frequency in the scan direction towards a longer wavelength. One kind of thermal feedback is established as resonance locked to the pump laser passively. As a result, the Lorentz-shaped adiabatic resonance is distorted to a thermal triangular,[31] as shown in Fig. 1(b). Because of this thermal effect, the pump can only be tuned gradually from short wavelength to intracavity mode. Conversely, if the pump is tuned from red detuned, the coupling to resonance is unstable. The dashed lines I, IV and V in Fig. 1(b) indicate the positions of pump at different stages relative to intracavity mode during the pump tuned from blue detuning to intracavity mode for FWM.

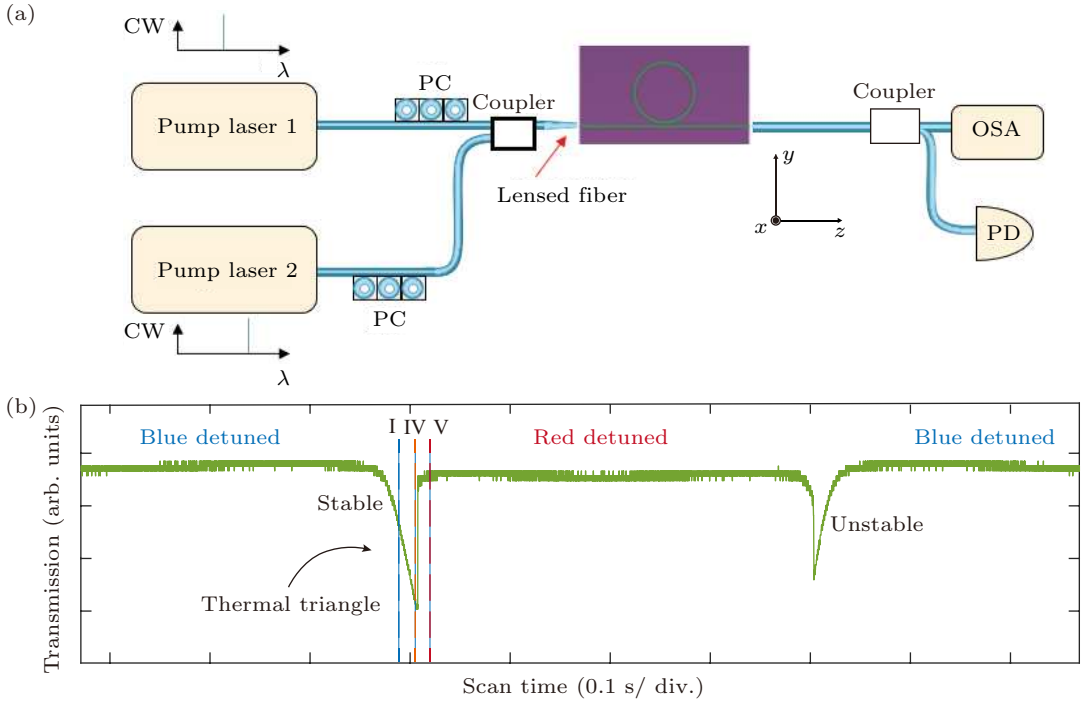


Fig. 1. (a) Experimental setup. PC: polarization controller; PD: photodetector; OSA: optical spectrum analyzer. The coordinate system in the figure corresponds to the actual crystallographic. Inset: schematic of waveguide cross section. (b) Forward and backward laser-scanned (0.1 nm/s) transmission spectrum near 1602 nm, under 4 mW pumping. The effective resonance is distorted as a triangular shape called thermal triangular due to thermal absorption. The dashed lines I, IV and V in the figure indicate the three relative positions of the pump in the resonance, respectively.

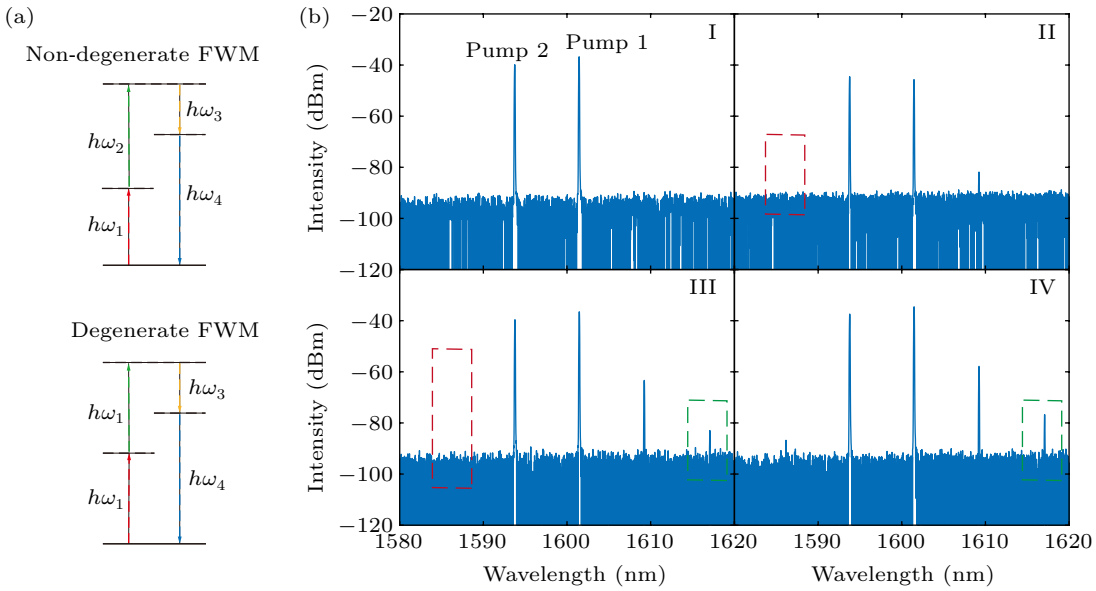


Fig. 2. (a) Illustration of annihilation (upward pointing arrows) and creation (downward pointing arrows) of photons in nondegenerate and degenerate four-wave mixing processes. The length of the arrows corresponds to the energy of photons. (b) Spectra of four stages (I–IV) in FWM with two pumps (pump 1 and pump 2) which correspond to two adjacent intracavity modes, during two CW pumps tuning from blue detuning to effective zero detuning of resonances. The red dashed boxes in stages II and III indicate the position of suppressed sideband in the FWM process. The rightmost sideband (inside green dashed boxes) in stages III and IV is generated by cascaded FWM. Stage IV indicates that when the two pumps are completely coupled into the intracavity modes.

FWM can be divided into nondegenerate and degenerate processes, as shown in Fig. 2(a). The corresponding nonlinear polarization are

$$P_{\mathrm{NL}}^{\mathrm{non}} = 6\varepsilon_0\chi^{(3)}E_1E_2E_3^*\,\mathrm{e}^{\mathrm{i}(k_1+k_2-k_3)z}\,\mathrm{e}^{-\mathrm{i}(\omega_1+\omega_2-\omega_3)t}, \quad (1)$$

$$P_{\mathrm{NL}}^{\mathrm{de}} = 3\varepsilon_0\chi^{(3)}E_1^2E_3^*\,\mathrm{e}^{\mathrm{i}(2k_1-k_3)z}\,\mathrm{e}^{-\mathrm{i}(2\omega_1-\omega_3)t}. \quad (2)$$

Here E_i represents the strength of applied optical field, and k_i is the corresponding wavevector, where $i = 1, 2, 3$. $\chi^{(3)}$ is known as the third-order nonlinear susceptibility and ε_0 is the permittivity of free space. To achieve maximum conversion efficiency, energy conservation between pump and signal should be satisfied, as well as phase matching, like $k_1 + k_2 - k_3 = k_4$ for nondegenerate four-wave mixing. In the experiment, two pumps (intrinsic linewidth is ~ 150 MHz) are coupled into two adjacent intracavity modes assisted by a photodetector slowly from blue detuning, for self-locking into the thermal triangular induced by thermal effect. Meanwhile, the other pump-induced change in refractive index, affects the detuning of the respective parties. After the pumps are all roughly tuned into the resonances, as shown by dashed line I in Fig. 1(b), there is no sideband generated in Fig. 2(b) (stage I) since the intracavity energy is low and the phase is remarkably mismatched. With two pumps (1, 2) tuned to long wavelength gradually, the first sideband in red wavelength is obtained, as shown in stage II in Fig. 2(b), while there is supposed to be one sideband on the symmetrical side (red dashed box) based on the two conservations. The sideband intensity is not high, due to weak interaction between pumps and cavity modes. Continue to tune the pumps to slight detuning, and a new sideband (in green dashed box), generated by cascaded FWM on the red side, as shown in stage III of Fig. 2(b), while the suppressed sideband on the blue side is still missing. Stage IV depicts the spectrum when both pumps are in zero detuning to the resonances, as the dashed line IV in Fig. 1(b). At this moment, the alterations of refractive index caused by thermal and photorefractive effect in the LN ring tend to be stable, pumps can be fully coupled into the cavity mode stably, the energy in the cavity is high and the phase is matched. However, the suppressed sideband is not released obviously besides the intensity of sidebands generated in previous stages enhanced. Further tuning to the red of pumps will break down the self-locked dynamic, so that no energy is coupled into the cavity instantly and all sidebands are eliminated, as the dashed line V in Fig. 1(b).

Generally speaking, non-degenerate FWM is easy to be implemented because of the small interval of each component, which can be regarded as zero dispersion. However, for 1-THz-FSR rings, the cavity mode spacing is too large to smash the effect of group velocity dispersion. The presence of dispersion makes the actual resonances not exactly equidistant, and their angular frequencies satisfy

$$\begin{aligned}\omega_\mu &= \omega_0 + D_1\mu + \frac{D_2}{2!}\mu^2 + \frac{D_3}{3!}\mu^3 + \cdots \\ &= \omega_0 + D_1\mu + D_{\mathrm{int}}(\mu), \end{aligned} \quad (3)$$

$$D_i = \left.\frac{\partial^i\omega_\mu}{\partial\mu^i}\right|_{\mu=0}, \quad (4)$$

where ω_0 is the frequency of the resonant field corresponding to the pump, and μ is the relative mode number counted with ω_0. $D_1/2\pi$ is the FSR of the cavity around the pump

frequency ω_0, for FSR varies with mode number influenced by dispersion. $D_2/2\pi$ is the walk-off of resonances from an equidistant resonance grid spaced by D_1, which directly and mainly reflects the group velocity dispersion of the mode, satisfying

$$D_2 = \omega_{+1} - 2\omega_0 + \omega_{-1} = -\beta_2 D_1^2/\beta_1, \tag{5}$$

where β_1 is the reciprocal of group velocity, and β_2 is the derivative of group velocity with respect to angular frequency, called group velocity dispersion. D_2 and higher-order dispersion D_i ($i \geq 3$) account for the integrated dispersion $D_{\rm int}$. From the cavity transmission spectrum in Fig. 3(a), it can be seen that there are two mode families in the cavity with different FSR, which will induce an avoided-mode crossing at a certain frequency. Limited by the gap between the bus waveguide and ring, 800 nm, the scanning wavelength starts from $\sim$ 1569 nm. Considering the FSR of the ring is $\sim$ 1 THz, and the purpose of dispersion fitting is to find an avoided-mode crossing point, the instability of CW laser can be neglected in this experiment.

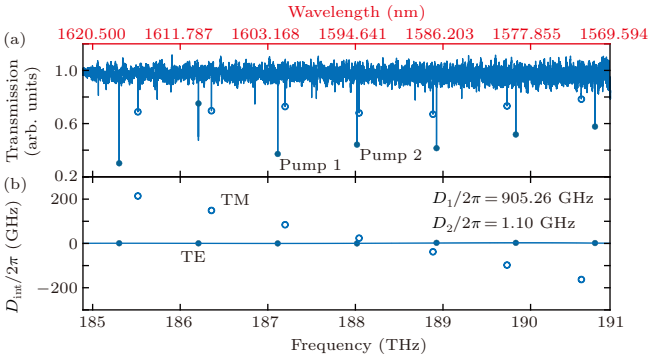


Fig. 3. (a) Normalized cavity transmission spectrum with solid circles denoting TE mode and hollow circles denoting TM mode. (b) The dispersion $D_{\rm int}/2\pi$ of TE mode. The solid circles correspond to the TE mode in panel (a), and the blue line is a fourth-order dispersion fitting.

Previously, it was thought that in a perfect isotropy resonator without any defect from fabrication, this crossover could be eliminated for cavity eigenmodes that are orthogonal and there is no interaction between them. By comparing the shape of the transmission spectra of these two mode families under the high power TE pump, we find that resonances of the mode with higher transmittance (the hollow circle) do not show triangular distortion caused by thermal effect. Thus, we judge this mode to be TM mode with orthogonal polarization of pump (TE), which is consistent with previous reports of both TE and TM modes supported in birefringent resonators.[6–9] The integrated dispersion $D_{\rm int}(\mu)$ of TE mode (solid line) in Fig. 3(b) is fitted by Eq. (3) with fourth-order dispersion from a uniform FSR ($D_1/2\pi \approx 905.32$ GHz) of TE mode. The positive $D_2/2\pi \approx 1.10$ GHz shows this waveguide possesses an anomalous dispersion, which is essential for a soliton formation. It is clear that an avoided-mode crossing occurs between pump 2 and its right cavity mode (blue-wavelength side), giving the reason why one sideband of a pair is suppressed in stages II and III of nondegenerate FWM depicted in Fig. 2(b).

Next, we will analyze the origin of this mode crossing, the hypothesis of the coexistence of TE and TM modes in X-cut LN microrings under TE or TM pump. In X-cut LN microcavities, the optical axis Z lies in the plane, as shown in the coordinate system of Fig. 1(a), so the effective refractive index of TE mode in the cavity is[32,33]

$$n_{\rm eff}(\theta) = \frac{n_{\rm o} n_{\rm e}}{\left(n_{\rm o}^2 \sin^2\theta + n_{\rm e}^2 \cos^2\theta\right)^{1/2}}, \tag{6}$$

within the interval $[n_{\rm e}, n_{\rm o}]$. θ is the angle between the optical axis and the wavevector. $n_{\rm o}$ and $n_{\rm e}$ denote the effective refractive indices of ordinary and extraordinary waves in LN crystal, respectively, which can be simulated by setting isotropic material properties in COMSOL, as shown in Fig. 4(a). For TM mode, the polarization direction is always parallel to the X axis, so its effective index is the index of the ordinary wave, $n_{\rm o}$. From Fig. 4(a), it is depicted that the effective refractive index of TM mode lies between $n_{\rm o}$ and $n_{\rm e}$ of TE mode after the crossing at 180 THz, the green region, indicating that TM mode will be bound to have the same effective index as the TE mode at 4 azimuths of the ring, according to Eq. (6), where these two orthogonal modes have strong interaction and polarization conversion. For example, the blue line in Fig. 4(b) is the effective index of pump 2 as a function of angle, while the red line shows that of TM mode. In this simulation, the material definition is isotropy, so that the effective $n_{\rm o}$ and $n_{\rm e}$ can be calculated and then substituted into Eq. (6) to present the effective index of TE mode. The intersections near $\theta = \pm\pi/2$ suggest that here the polarization is converted, and the TM mode will be stimulated when it resonates in the cavity. As the FSR mismatch of TE and TM mode, there will be an avoided-mode crossing around one certain resonance. Thus, it will suppress the generation of one sideband of FWM and disrupt the formation of cascaded FWM, which will also impose a negative effect on the formation of soliton. Insets in Fig. 4(a) display the electric field distribution of TE and TM modes of the microring in our experiment under isotropic material definition. Although it has been reported that mode coupling between various orders of TE modes may occur in LN waveguides, the conversion efficiency or crosstalk is about 10 dB to 20 dB.[13,14] In our experiment, shown in Fig. 3(a), there is a broadband conversion with about a twofold difference between TE and TM modes, where TM modes have weaker coupling between bus waveguide and ring, so the mode-order conversion can be neglected as well as polarization conversion with TM modes.

In isotropic materials, it is easy to calculate the eigenmodes and mode crossing point by calculating the effective re-

fractive indices of TE and TM modes then substituting them to resonance conditions. However, this practice doesn't apply to TE modes in X-cut rings due to birefringence, while it is feasible for TM modes. By anisotropic material definition, it may be possible to simulate in COMSOL by 3D modal. Therefore, one effective 2D modal is proposed to predict the position of the unavoidable avoided-mode crossing. Here, the microring is regarded as a straight waveguide with periodic boundaries. Periodicity is the circumference of a ring, and the birefringence is replaced by an effective index equation in Fig. 4(c), a function of x, where $x = \theta r$ denotes the propagation distance of light within the ring. Since the 2D model simplifies the field distribution in the z-direction, infinite waveguide width, the length of a straight waveguide is different from that of ring. So, we use the equivalent circumference of 26.1 μm in our simulation. In order to preserve the influence of substrate (SiO_2) and air on the mode distribution as much as possible, we analyze the eigenmodes from the profile as depicted in Fig. 4(c). In the Y-axis direction, the effective index is defined as n_o, and in the Z-axis direction, that is similar to Eq. (6) but with a $\pi/2$ shift. Figure 4(c) shows the eigenmodes distribution of TE (187.92 THz) and TM (187.95 THz) and their field components at z and y direction, respectively. The calculated resonances are plotted in Fig. 4(d) without considering dispersion, which agrees with the experimental results in Fig. 3(b) well.

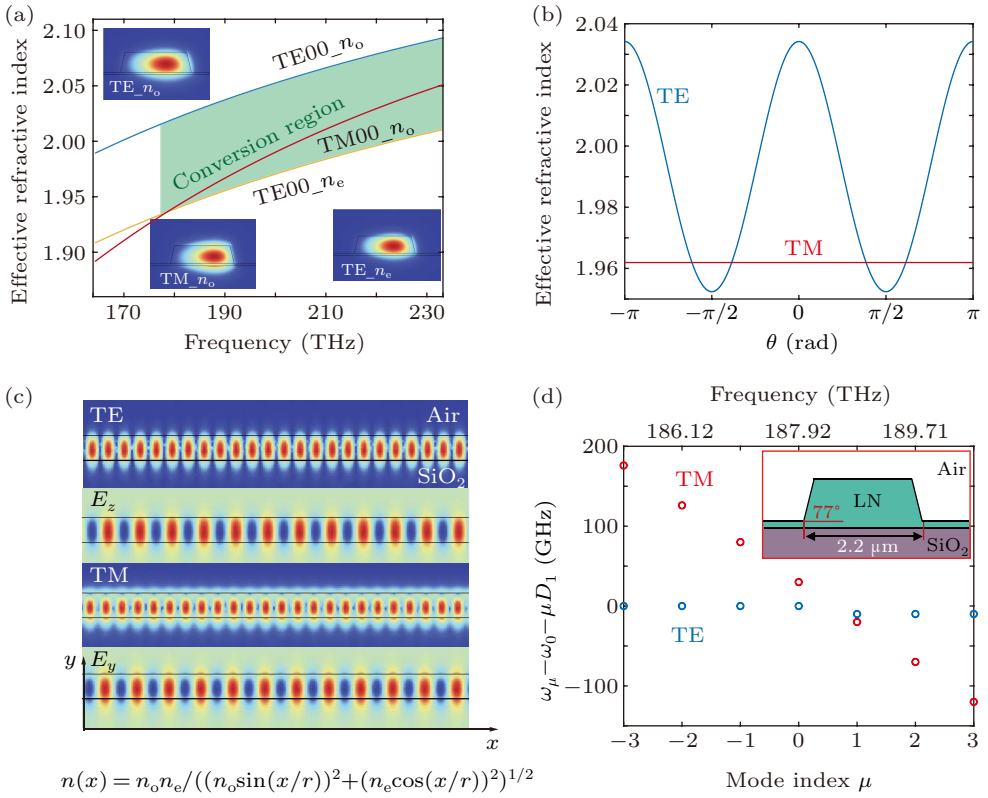


Fig. 4. Analysis of the polarization conversion of TE and TM modes in X-cut rings. (a) The effective refractive index of TE mode propagating along the extraordinary (TE_n_e) and ordinary (TE_n_o) axis and that of TM mode along the ordinary axis (TM_n_o) in the ring, was obtained by COMSOL simulation. Green region shows the range where polarization conversion happened. (b) Effective refractive index changes versus angle for TE mode in the cavity at 1594 nm pump (blue line), pump 2, and the index for TM mode (red line). (c) 2D modal for simulating eigenmodes of X-cut rings. The microring is equated to a straight waveguide with periodic boundaries and periodic variations of refractive index. The Y-axis, from bottom to top, represents substrate (SiO_2), LN, and air. (d) Simulated cavity resonances (eigenmodes of the waveguide), TE (blue) and TM (red), and avoided-mode crossing in the frame of TE mode. The pump is at 187.92 THz. Dispersion is neglected here.

3. Conclusion and perspectives

We study the polarization conversion in 1-THz-FSR lithium niobate rings and find that in addition to the geometric structure and scattering of annular waveguides, the natural property of the periodic fluctuation of mode effective index with angle in birefringent crystals can cause the conversion between TE and TM modes, with multiple-resonance condition. This mechanism makes the coexistence of these two orthogonal modes in X-cut LN microrings unavoidable, as well as the avoided-mode crossing between these two mode families due to FSR mismatch. The induced mode crossing will distort the dispersion heavily,[34] which suppresses one sideband of the local nondegenerate FWM and the cascaded FWM later, imposing a disruption on the formation of soliton possibly. Then to calculate the mode crossing point, we propose a 2D method by stretching the ring to a straight waveguide with periodic boundaries and periodic variation of the effective index. Simulated resonances agree reasonably well with the experiment

by this method. This work paves the way for future theoretical research and applications of polarization conversion in birefringent waveguides, like calculating conversion efficiency by coupled-mode equation and designing a mode converter just by a short-curved waveguide with a small footprint. For example, it will provide suggestions for the new design of entirely integrated polarization converters, which can be embed in quantum circuits, simulation on the birefringent platform and may be helpful for the formation of soliton in X-cut LN microrings.

Acknowledgments

We thank Weimin Ye, Ning Liu, Jipeng Xu and Xingqiao Chen for valuable discussions during the preparation of this manuscript. Project supported by the National Natural Science Foundation of China (Grant Nos. 12274462 and 11674396), the Department of Science and Technology of Hunan Province of China (Grant Nos. 2017RS3039 and 2018JJ1033), and the Hunan Provincial Innovation Foundation for Postgraduate of China (Grant No. QL20210006).

References

[1] Grady N K, Heyes J E, Chowdhury D R, Zeng Y, Reiten M T, Azad A K, Taylor A J, Dalvit D A R and Chen H T 2013 *Science* **340** 1304
[2] Shi Z, Zhu A Y, Li Z, Huang Y W, Chen W T, Qiu C W and Capasso F 2020 *Sci. Adv.* **6** 3367
[3] Balthasar Mueller J P, Rubin N A, Devlin R C, Groever B and Capasso F 2017 *Phys. Rev. Lett.* **118** 113901
[4] Chen H, Wang J, Ma H, Qu S, Xu Z, Zhang A, Yan M and Li Y 2014 *J. Appl. Phys.* **115** 154504
[5] Wang J, Bonneau D, Villa M, Silverstone J W, Santagati R, Miki S, Yamashita T, Fujiwara M, Sasaki M, Terai H, Tanner M G, Natarajan C M, Hadfield R H, O'Brien J L and Thompson M G 2016 *Optica* **3** 407
[6] Melloni A, Morichetti F and Martinelli M 2004 *Opt. Lett.* **29** 2785
[7] Morichetti F, Melloni A and Martinelli M 2006 *J. Lightwave Technol.* **24** 573
[8] Ramelow S, Farsi A, Clemmen S, Levy J S, Johnson A R, Okawachi Y, Lamont Michael R E, Lipson M and Gaeta A L 2014 *Opt. Lett.* **39** 5134
[9] Weng W and Luiten A N 2015 *Opt. Lett.* **40** 5431
[10] Ke L, Rajagopal S R and Rosenberger A T 2021 *Phys. Rev. A* **104** 053534
[11] Pan A, Hu C, Zeng C and Xia J 2019 *Opt. Express* **27** 35659
[12] Wang J, Chen P, Dai D and Liu L 2020 *IEEE Photonics J.* **12** 1
[13] Ma M, Yuan M, Zhou X, Xiao H, Cao P, Cheng L, Nguyen T G, Boes A, Ren G, Su Y, Mitchell A and Tian Y 2023 *Laser Photonics Rev.* **17** 2200862
[14] Zhao W, Liu R, Zhu M, Guo Z, He J, Li H, Pan B, Yu Z, Liu L, Shi Y and Dai D 2023 *Laser Photonics Rev.* **17** 2200774
[15] Levy M, Osgood R M, Liu R, Cross L E, Cargill G S, Kumar A and Bakhru H 1998 *Appl. Phys. Lett.* **73** 2293
[16] Rabiei P and Gunter P 2004 *Appl. Phys. Lett.* **85** 4603
[17] Zhang M, Wang C, Cheng R, Shams-Ansari A and Lončar M 2017 *Optica* **4** 1536
[18] Desiatov B, Shams-Ansari A, Zhang M, Wang C and Lončar M 2019 *Optica* **6** 380
[19] Wolf R, Breunig I, Zappe H and Buse K 2018 *Opt. Express* **26** 19815
[20] Lin J, Bo F, Cheng Y and Xu J 2020 *Photonics Res.* **8** 1910
[21] Gao R, Yao N, Guan J, Deng L, Lin J, Wang M, Qiao L, Fang W and Cheng Y 2022 *Chin. Opt. Lett.* **20** 011902
[22] Zhu D, Shao L, Yu M, Cheng R, Desiatov B, Xin C J, Hu Y, Holzgrafe J, Ghosh S, Shams-Ansari A, Puma E, Sinclair N, Reimer C, Zhang M and Lončar M 2021 *Adv. Opt. Photonics* **13** 242
[23] Wang C, Zhang M, Chen X, Bertrand M, Shams-Ansari A, Chandrasekhar S, Winzer P and Lončar M 2018 *Nature* **562** 101
[24] He M, Xu M, Ren Y, Jian J, Ruan Z, Xu Y, Gao S, Sun S, Wen X, Zhou L, Liu L, Guo C, Chen H, Yu S, Liu L and Cai X 2019 *Nat. Photonics* **13** 359
[25] Rao A, Patil A, Rabiei P, Honardoost A, DeSalvo R, Paolella A and Fathpour S 2016 *Opt. Lett.* **41** 5700
[26] Chang L, Li Y, Volet N, Wang L, Peters J and Bowers J E 2016 *Optica* **3** 531
[27] Wang C, Langrock C, Marandi A, Jankowski M, Zhang M, Desiatov B, Fejer M M and Lončar M 2018 *Optica* **5** 1438
[28] Wang C, Zhang M, Yu M, Zhu R, Hu H and Loncar M 2019 *Nat. Commun.* **10** 978
[29] Zhang M, Buscaino B, Wang C, Shams-Ansari A, Reimer C, Zhu R, Kahn J M and Lončar M 2019 *Nature* **568** 373
[30] Kang S, Lv X, Yang C, Ma R, Gao F, Yu X, Bo F, Zhang G and Xu J 2024 *Materials* **17** 1190
[31] Carmon T, Yang L and Vahala K J 2004 *Opt. Express* **12** 4742
[32] Lin J, Xu Y, Ni J, Wang M, Fang Z, Qiao L, Fang W and Cheng Y 2016 *Phys. Rev. Appl.* **6** 014002
[33] Lin J, Yao N, Hao Z, Zhang J, Mao W, Wang M, Chu W, Wu R, Fang Z, Qiao L, Fang W, Bo F and Cheng Y 2019 *Phys. Rev. Lett.* **122** 173903
[34] Herr T, Brasch V, Jost J D, Wang C Y, Kondratiev N M, Gorodetsky M L and Kippenberg T J 2014 *Nat. Photonics* **8** 145